


# Analytical analysis of the generation of a rotating driving magnetic field on the outer surface of a magnetic pinch load with a helical return current post

Shu-Chao Duan,\* Ge-Guang He, Shao-Tong Zhou, Ming-Xian Kan, and Gang-Hua Wang  
*Institute of Fluid Physics, China Academy of Engineering Physics, Mianyang 621999, China*

 (Received 19 May 2023; revised 23 December 2023; accepted 22 February 2024; published 19 March 2024)

A recently emerging approach adopts a directionally time-varying (rotating) magnetic field to drive a pinch load, aiming to mitigate the inherent magneto-Rayleigh-Taylor instability in dynamic  $Z$  pinches. A helical return current post (RCP) serves as a functional structural element capable of generating the requisite driving magnetic field for this purpose in the load region. This paper first calculates the current azimuthally induced on the outer surface of a magnetically pinched load within this type of RCP using a zero-dimensional lumped-parameter circuit model. The results show that the induced current deviates significantly from the presumed “perfect” induced current (100% amplitude) as reported in the literature [S. A. Sorokin, *Plasma Phys. Rep.* **39**, 139 (2013); P. F. Schmit *et al.*, *Phys. Rev. Lett.* **117**, 205001 (2016); G. A. Shipley *et al.*, *Phys. Plasmas* **26**, 102702 (2019); and P. C. Campbell *et al.*, *Phys. Rev. Lett.* **125**, 035001 (2020)], with an effective coefficient of current induction considerably less than 1. However, even when the load is fully compressed to the axis, the effective coefficient does not approach zero but rather converges to a finite value that solely depends on the aspect ratio of the RCP. This is quite favorable for the suppression of magneto-Rayleigh-Taylor instability in the  $Z$  pinch. As for the pointlike  $X$  pinch, the axial magnetic field does not tend to zero but a finite value, though the effective coefficient tends to zero, and this result may be used to suppress the instability in  $X$  pinch and improve the time stability and spatiotemporal unity of hot spots. In addition, the anode and cathode plates have the potential to enhance the current induced in the load. This paper then analyzes the axial distribution and time behavior of the induced current adopting an approximate analytical method and numerical integration and finds an approximate invariance that can be well characterized by  $\delta t$ , the product of the normalized skin depth and time. Similar values of  $\delta t$  indicate similar axial distribution characteristics. When  $\delta t$  is lower than, at, or higher than the critical region ( $\sim 0.1$ – $0.3$ ), the axial distribution appears dumbbell shaped, nearly flat, and arched, respectively. These distributively induced currents can be exploited to achieve quasispherical, near flat, and dumbbell-shaped implosions, respectively.

DOI: 10.1103/PhysRevAccelBeams.27.030401

## I. INTRODUCTION

Dynamic  $Z$  pinches [1–3] can be used to inertially confine fusion plasmas and to generate x-ray radiation of the highest intensity in laboratories. Their applications in fusion energy, high-tech national defense, and economic industries hold immense value. However, they face a critical obstacle in the form of magneto-Rayleigh-Taylor (MRT) instability [4–7].

It is widely known that a magnetic field has an inhibitory effect on instability modes having wave vectors that are not perpendicular to the field (i.e., wave vectors that have

nonzero parallel components). Conversely, a magnetic field does not inhibit modes that are perpendicular to it. In the standard  $Z$ -pinch configuration, the MRT instability features a mode perpendicular to the driving magnetic field. The growth rate of the MRT instability thus remains completely unaffected by the magnetic field, with a formula identical to that for the classical fluid Rayleigh-Taylor instability. In addition, magnetic shear reduces the growth rate of the MRT instability. Both the inhibitory effect of a magnetic field on nonperpendicular modes and that of magnetic shear are realized through the component of the magnetic field parallel to the wave vector, suggesting that work is required to bend magnetic field lines. The second-order differential equation for eigenvalues [1] derived from normal mode analysis includes a  $F^2 = (k \cdot B)^2 = k^2 B_{\parallel}^2$  term, where  $k \cdot B$  is the result of the action of  $B \cdot \nabla$  on the perturbation quantity and represents the bending of magnetic field lines by perturbations in the direction of the magnetic field. Therefore, the  $F$  term generally has a

\*Corresponding author: s.duan@163.com

Published by the American Physical Society under the terms of the *Creative Commons Attribution 4.0 International license*. Further distribution of this work must maintain attribution to the author(s) and the published article's title, journal citation, and DOI.

stabilizing effect. It is anticipated that the magnetic field exerts an inhibitory effect on any mode (with wave vector  $k$ ) for which the time-averaged  $F^2$  is positive.

It is thus worth considering the use of a directionally time-varying (rotating) driving magnetic field to suppress MRT instability in dynamic Z pinches [8–12]. In this scheme, the direction of the driving magnetic field rotates over time and, on a time average basis, meets the condition that  $F^2 > 0$  for all modes, and it is thus expected that this driving method suppresses the instability of all modes. If an axial magnetic field is added on the inner side of the liner, it will be enhanced through the conservation of magnetic flux during the implosion process. Such an axial magnetic field can also suppress MRT instability through the mechanisms of magnetic shear and reduced implosion acceleration. These two strategies are mutually complementary and can be applied individually or in combination. A comprehensive review of many other possible methods of inhibiting MRT instability can be found in Ref. [2].

The technique using a helical return current post (RCP) to generate an axial magnetic field through electromagnetic induction on the outer surface of the magnetic pinch load was originally proposed in [13–15]. Subsequent literature related to this configuration includes [10,16–19]. Taking a slightly different approach, some studies, including [20–24], have proposed the technique using the spiral current channel on the load to generate an axial magnetic field. The first technique is the most relevant to this article, which involves a helical RCP whose structure is shown in Fig. 1. The helical structure generates an azimuthal ( $\ominus$ ) component of the loading current flowing through the RCP. This current component induces an azimuthal current on the outer surface of the magnetic pinch load, corresponding

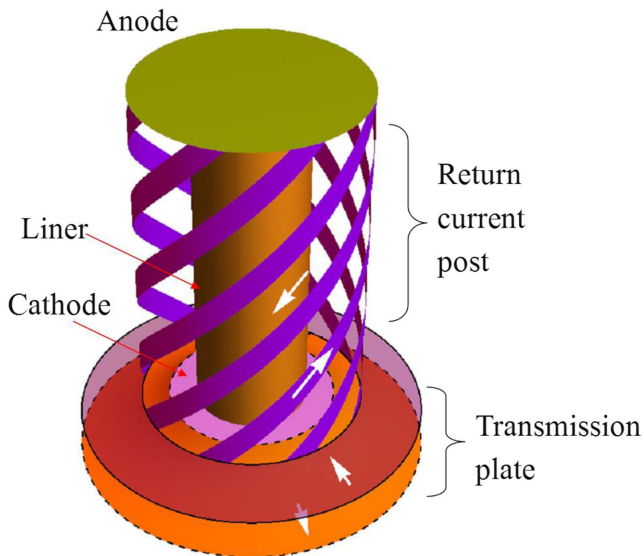


FIG. 1. Schematic of a helical RCP configuration. The white arrows indicate the direction of current; i.e., the direction opposite the electron flow.

to an axial magnetic-field component. Naturally, there also exists an azimuthal magnetic-field component (provided by the axial current) on the outer surface of the magnetic pinch load. These two magnetic-field components do not evolve synchronously, leading to dynamic variations in the direction of the overall driving magnetic field on the outer surface of the load.

This study adopts a zero-dimensional lumped-parameter circuit (LPC) model to calculate the current azimuthally induced on the outer surface of the load in such a configuration and analyzes the axial distribution and time behavior of the induced current adopting an approximate analytical method and numerical integration. Once the azimuthal current is determined, the axial magnetic field and overall driving magnetic field are straightforward to calculate. Accurately calculating currents, particularly, the azimuthally induced current, is important to the dynamic analysis and instability assessment of magnetic pinches. In this paper, it is found that the induced current is far different from the “ideal” induction assumed in the literature. The nonideal induced current reduces the effective convergence ratio from both dynamics and integrity aspects. The effective convergence ratio refers to the convergence ratio under the condition that the integrity of the liner is maintained. Compared with the ideal case, the discounted nonideal induced current first reduces the implosion power and thus the degree of compression and second reduces the suppression of the instability, resulting in the integrity of the liner being reduced earlier or destroyed more easily. A reduction in the effective convergence ratio in turn naturally reduces the fusion gain. The reduction mentioned here is relative to ideal induction. Fortunately, the discount of the nonideal induction does not reach zero. In this way, relative to the traditional standard Z pinch, there are improvements in the implosion dynamics, liner integrity, instability suppression, and fusion gain. In terms of the instability, the accuracy of the induced current is very important as it relates to both the acceleration and speed of the implosion and the direction of the driving magnetic field. It is known from elementary RT instability theory that the implosion acceleration directly affects the growth of MRT instability. In the case that the radial convergence effect, namely the Bell-Plesset effect [25], is considered for a cylindrical or spherical configuration, the implosion speed also affects the growth of instability; i.e., the perturbation equation contains a term proportional to  $\dot{R}/R$ , where  $R$  is the liner radius and the dot stands for the differential with respect to time. The speed and degree of change in the direction of the driving magnetic field directly and significantly affect the suppression of the MRT instability [11,12].

## II. LPC MODEL

In electromagnetic loading with a helical RCP structure, a Z pinch, in fact, entails a combination of an azimuthal

pinch ( $\Theta$  pinch) and an axial pinch ( $Z$  pinch). In the preliminary stage of the present study, the analysis is simplified by decoupling the  $Z$  pinch and focusing solely on the azimuthal pinch. In addition, it is assumed that the load experiences minimal motion, allowing for isolation and examination of its electromagnetic behavior. This approach is particularly applicable to the early and intermediate stages of a magnetic pinch. In the later stages, the  $Z$  pinch undergoes substantial motion, necessitating the coupling of electromagnetic and dynamic behaviors.

The azimuthal current component in the helical RCP structure provides an azimuthal pinch, which is essentially an electromagnetic induction process. This process is approximately described by adopting an LPC model:

$$\begin{aligned} \frac{d\Phi}{dt} &= -RI_{\Theta}, \\ \Phi &= LI_{\Theta} + MI_P, \end{aligned} \quad (1)$$

where  $I_P$  is the azimuthal current component in the helical RCP, which is treated as a known quantity determined by partitioning a fraction of the total driving current based on the tilt ratio of the helical RCP. In practice, the total driving current is typically obtained through diagnostics.  $M$  is the mutual inductance of the load and RCP, which is associated with the azimuthal current.  $\Phi$  is the axial magnetic flux on the load, namely the integral of the axial magnetic field  $B_z$  in the  $r-\theta$  section (a circular area) on the magnetic pinch load.  $I_{\Theta}$  is the azimuthal induced current on the load, and its positive direction is specified here to be the same as that of  $I_P$ . This treatment is in contrast with that reported in a previous study [26].  $R$  and  $L$  are the resistance and inductance associated with the azimuthal induced current. The electromagnetic induction is the predominant factor considered, whereas the effect of resistance can be further neglected without appreciably affecting the primary conclusions.

### III. CALCULATION OF INDUCTANCE AND MUTUAL INDUCTANCE

It is difficult to strictly consider the helicity (i.e., inclination angle and pitch) of the coils when calculating the inductance of a solenoid. Therefore, the helicity of the coils is generally ignored in calculation; i.e., the inclination angle and pitch are assumed to be zero, as in the case of this paper. Therefore, the inclination angle and pitch are not included in the inductance formula. However, the effect of the inclination angle can be approximated; i.e., the current in a solenoid with a nonzero inclination angle is decomposed into axial and azimuthal components, and the latter is regarded as flowing through a solenoid with a zero inclination angle, while the effect of the inclination angle is introduced through the split proportion of the azimuthal current in the total current. This section involves the inductance and mutual inductance relating only to the

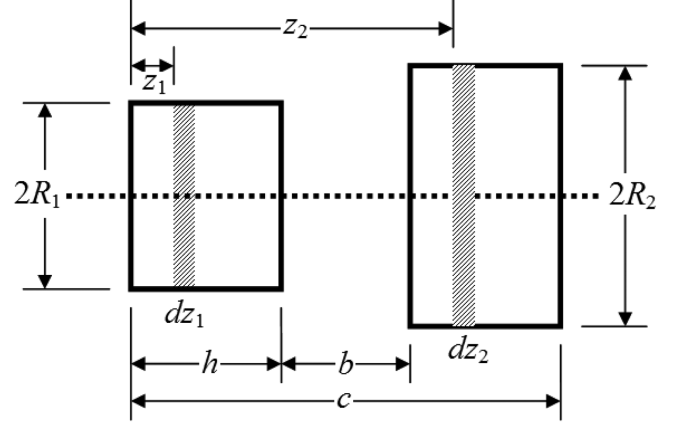


FIG. 2. Schematic of two coaxial solenoids. See the main text for the descriptions of the variables.

azimuthal current. The inclination angle is reintroduced in Sec. VII.

Suppose there are two coaxial cylindrical solenoids having radii  $R_1$  and  $R_2$  and  $m$  and  $n$  coil turns in their respective axial unit lengths. The axial length of the first solenoid is  $h$ , the proximal ends are axially separated by  $b$  ( $b > 0$  when there is no nesting and  $b < 0$  when there is nesting), and the distal ends are separated by  $c$ , as shown in Fig. 2.

We take one coil element for each of the two solenoids, with the axial coordinates being  $z_1$  and  $z_2$ , respectively. The mutual inductance of the two coil elements is

$$\bar{M} = \mu \sqrt{R_1 R_2} \left[ \left( \frac{2}{k_0} - k_0 \right) K[k_0^2] - \frac{2}{k_0} E[k_0^2] \right], \quad (2)$$

where  $K$  and  $E$  are the first and second types of the elliptic integral function, respectively, and  $k_0^2 = \frac{4R_1 R_2}{(z_1 - z_2)^2 + (R_1 + R_2)^2}$ .

The mutual inductance of the two solenoids is

$$M = \frac{1}{\iint dz_1 dz_2} \iint \bar{M} dz_1 dz_2. \quad (3)$$

After some transformations, the mutual inductance is expressed as [27]

$$\begin{aligned} M &= \sum_{i=1}^4 M_i = \sum_{i=1}^4 (-1)^i \frac{\sqrt{R_1 R_2} D k^2}{2k_i} S_i \\ &= \sum_{i=1}^4 (-1)^i \frac{\sqrt{R_1 R_2} D k^2}{2k_i} \int_0^{\pi/2} \frac{\sqrt{1 - k_i^2 \sin^2 \theta}}{1 - k^2 \sin^2 \theta} \sin^2 2\theta d\theta, \end{aligned} \quad (4)$$

where

$$\begin{aligned}
D &= 2\mu R_1 R_2 m n, \\
k^2 &= \frac{4R_1 R_2}{(R_1 + R_2)^2}, \\
k_1^2 &= \frac{4R_1 R_2}{(R_1 + R_2)^2 + (h - c)^2}, \\
k_2^2 &= \frac{4R_1 R_2}{(R_1 + R_2)^2 + c^2}, \\
k_3^2 &= \frac{4R_1 R_2}{(R_1 + R_2)^2 + (h + b)^2}, \\
k_4^2 &= \frac{4R_1 R_2}{(R_1 + R_2)^2 + b^2}. \tag{5}
\end{aligned}$$

The integral part of Eq. (4) is expressed using a general special function as

$$\begin{aligned}
S_i &= \int_0^{\pi/2} \frac{\sqrt{1 - k_i^2 \sin^2 \theta}}{1 - k^2 \sin^2 \theta} \sin^2 2\theta d\theta \\
&= \frac{4}{\sqrt[3]{1 - k_i^2 k_i^2 k^6}} \left( [k^4(1 - k_i^2) - 3k_i^4(1 - k^2)] K \left[ \frac{k_i^2}{-1 + k_i^2} \right] \right. \\
&\quad + (1 - k_i^2) k^2 (k_i^2(3 - k^2) - k^2) E \left[ \frac{k_i^2}{-1 + k_i^2} \right] \\
&\quad \left. + 3k_i^2(k_i^2 - k^2) Pi \left[ \frac{k^2}{-1 + k^2}, \frac{k_i^2}{-1 + k_i^2} \right] \right), \tag{6}
\end{aligned}$$

where  $Pi$  denotes elliptic integral functions of the third kind. Using the identities

$$\begin{aligned}
E \left[ -\frac{x}{1-x} \right] &= E[x] / \sqrt{1-x} \\
K \left[ -\frac{x}{1-x} \right] &= K[x] \sqrt{1-x} \\
Pi \left[ -\frac{x}{1-x}, -\frac{y}{1-y} \right] &= Pi[x, y] (1-x) \sqrt{1-y}, \tag{7}
\end{aligned}$$

Equation (6) is rewritten as

$$\begin{aligned}
S_i &= \frac{4}{3k_i^2 k^6} [[k^4(1 - k_i^2) - 3k_i^4(1 - k^2)] K[k_i^2] \\
&\quad + k^2(k_i^2(3 - k^2) - k^2) E[k_i^2] \\
&\quad + 3k_i^2(k_i^2 - k^2)(1 - k^2) Pi[k^2, k_i^2]]. \tag{8}
\end{aligned}$$

The mutual inductance is thus expressed as

$$\begin{aligned}
M &= \sum_{i=1}^4 (-1)^i \frac{2\sqrt{R_1 R_2 D}}{3k_i^3 k^4} ([k^4(1 - k_i^2) - 3k_i^4(1 - k^2)] K[k_i^2] \\
&\quad + k^2(k_i^2(3 - k^2) - k^2) E[k_i^2] \\
&\quad + 3k_i^2(k_i^2 - k^2)(1 - k^2) Pi[k^2, k_i^2]). \tag{9}
\end{aligned}$$

The parameters are taken as  $R_1 = R_2 = R$ ,  $-b = c = h$ , such that the two solenoids degenerate into the same solenoid. The mutual inductance formula in Eq. (9) then degenerates into an inductance (self-inductance) formula (as described in Eq. (15) in Ref. [27]):

$$L = \frac{2\mu R N^2}{3} \left( \frac{K[\frac{4R^2}{4R^2+h^2}]}{\sqrt{\frac{4R^2}{4R^2+h^2}}} + \frac{4R^2-h^2}{h^2} E[\frac{4R^2}{4R^2+h^2}] - \frac{4R^2}{h^2} \right), \tag{10}$$

where  $N$  is the number of turns in the solenoid. Commonly used software allows for the convenient use of general special functions. Equations (9) and (10) can thus be directly used in calculation. However, to facilitate comparison with the existing literature and address errors and flaws, approximations for the aforementioned expressions are provided below.

With a long solenoid approximation for the inductance equation ( $h > R_1, R_2$ ), expanding the exact expression of inductance in Eq. (10) in a series with a large  $h$  yields a highly accurate approximate expression:

$$L = \mu R N^2 \left( \frac{\pi R}{h} - \frac{8R^2}{3h^2} + \frac{\pi R^3}{2h^3} - \frac{\pi R^5}{4h^5} + O\left[\frac{1}{h}\right]^6 \right). \tag{11}$$

Equation (16) in Ref. [27] is consistent with Eq. (11), as the former corresponds to considering only the first two terms of the latter.

With a short solenoid approximation for the inductance equation ( $h < R_1, R_2$ ), expanding the exact expression of inductance in Eq. (10) in a series with a small  $h$  yields

$$L = \mu R N^2 \left( \ln\left(\frac{8R}{h}\right) - \frac{1}{2} + \frac{h^2}{32R^2} \left[ \frac{1}{4} + \ln\left(\frac{8R}{h}\right) \right] + O[h]^4 \right). \tag{12}$$

Equation (17) in Ref. [27], which corresponds to consider only the first two terms of Eq. (12), contains an error in its overall coefficient. The coefficient of  $2/3$  should be corrected to 1. An alternative expression is presented in Ref. [26] and aligns with the expression provided here. By introducing the definition  $q = \frac{h}{4R}$ , Eq. (12) is rewritten as

$$\begin{aligned}
L &= \mu R N^2 \left( \ln(2) - \frac{1}{2} - \ln(q) \right. \\
&\quad \left. + q^2 \left( \frac{1 + 4 \ln(2)}{8} - \frac{1}{2} \ln(q) \right) + O[q]^4 \right) \\
&\approx \mu R N^2 (0.193147 + 0.471574 q^2 \\
&\quad - \ln(q) - 0.5 q^2 \ln(q)). \tag{13}
\end{aligned}$$

Equation (B.1) in Ref. [26], which has a form similar to that of the expansion in Eq. (13) presented here, has differences in terms of its coefficients. Figure 3 compares

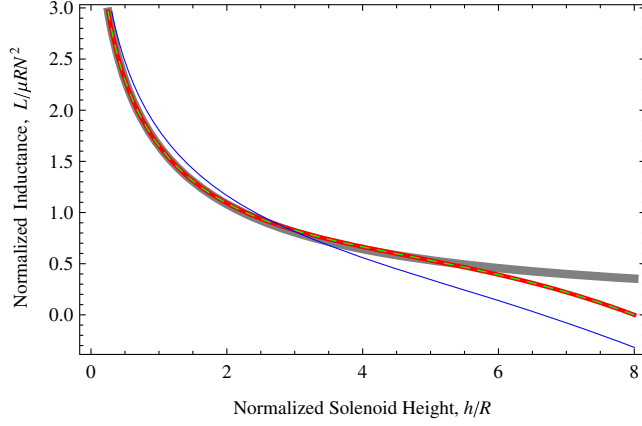


FIG. 3. Comparison of the approximate and exact expressions of inductance. Gray line: exact expression in Eq. (10). Red line: expansion in Eq. (13). Green dashed line: expansion in Eq. (13) (with truncated coefficients). Blue line: Eq. (B.1) in Ref. [26].

these approximate expressions. The gray line represents the exact expression given in Eq. (10) for inductance. The red line represents the expansion in Eq. (13), and the green

$$\begin{aligned}
 M &= \sum_{i=1}^4 (-1)^i \frac{\sqrt{R_1 R_2} D k^2}{2k_i} S_i \\
 &= \sum_{i=1}^4 (-1)^i \frac{\sqrt{R_1 R_2} D k^2}{2k_i} \pi \left\{ \left( \frac{1}{4} + \frac{k^2}{8} + \frac{5k^4}{64} + \frac{7k^6}{128} + O[k]^8 \right) + \left( -\frac{1}{16} - \frac{5k^2}{128} - \frac{7k^4}{256} - \frac{21k^6}{1024} + O[k]^8 \right) k_i^2 \right. \\
 &\quad \left. + \left( -\frac{5}{512} - \frac{7k^2}{1024} - \frac{21k^4}{4096} - \frac{33k^6}{8192} + O[k]^8 \right) k_i^4 + \left( -\frac{7}{2048} - \frac{21k^2}{8192} - \frac{33k^4}{16384} - \frac{429k^6}{262144} + O[k]^8 \right) k_i^6 + O[k_i]^8 \right\}. \quad (14)
 \end{aligned}$$

Equation (32) in Ref. [27] is similar to Eq. (14), but its coefficients are not as precise as those in Eq. (14), even within the given range of significant digits.

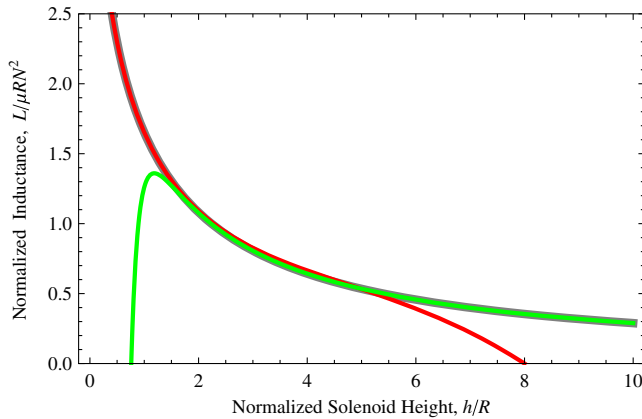


FIG. 4. Comparison of the approximate expressions for the inductance of the long and short solenoids with the exact expressions. Gray line: exact expression in Eq. (10). Red line: approximation for the short solenoid in Eq. (12) or (13). Green line: approximation for the long solenoid in Eq. (11).

dashed line represents the same expansion but with coefficients truncated to a certain number of significant digits. It is evident that the number of significant digits in the coefficients of the expansion is sufficient. The accuracy of this expansion is high in the region where  $h/R < 5$ . The blue line represents Eq. (B.1) in Ref. [26], which has a form similar to that of the expansion presented here. However, its coefficients are not accurate, leading to notable deviations from the exact values in the region, where  $h/R > 0.5$ .

The approximate expressions for the inductance of the long and short solenoids presented here have a remarkably high level of accuracy, and their usable ranges can be connected. As depicted in Fig. 4, if the approximate expression (12) or (13) for a short solenoid (red line) is used in the  $h/R \in (0, 1.88]$  area and the approximate expression (11) (green line) for the long solenoid is used in the  $h/R \in [1.88, \infty)$  area, then the error of this piecewise approximate expression relative to the exact expression (10) is less than 0.7% throughout the range of  $h/R \in (0, \infty)$ .

A series expansion of the mutual inductance in Eq. (9) ( $k_i \leq k \leq 1$  as a small parameter) is further presented

The above discussion focuses on the calculation of the mutual inductance (self-inductance) between two coaxial cylindrical solenoids with a small pitch (approaching zero). These calculations can be applied to the calculation of mutual inductance (self-inductance) in the context of the current induced by a helical RCP structure on the outer surface of a magnetic pinch load, which is of interest in this paper. For the specific problem in question, the anode and cathode plates, the end-feeding structure of the magnetic insulated transmission line (MITL), and the coupling of the axial currents are temporarily excluded from consideration. Furthermore, the axial distribution and radial penetration of the current are ignored. Thus the remaining system, comprising a pinch load and RCP, can be regarded as two coaxial solenoids with closely spaced turns (i.e., a small pitch). These solenoids have the same height  $h$  and the radii  $R_1$  and  $R_2$ . Therefore,  $b = -h$ ,  $c = h$ ,  $m = n = 1/h$ . We then have  $k_1^2 = k_3^2 = k^2 = \frac{4R_1 R_2}{(R_1 + R_2)^2}$ ,  $k_2^2 = k_4^2 = \frac{4R_1 R_2}{(R_1 + R_2)^2 + h^2}$ ,  $M_1 = M_3$ , and  $M_2 = M_4$ . Hence,  $M = 2(M_1 + M_2)$ ; i.e.,

$$\begin{aligned}
M &= 2 \sum_{i=1}^2 M_i \\
&= \frac{2\mu(R_1 + R_2)}{3h^2} ((R_1 - R_2)^2 K[k_1^2] - (R_1^2 + R_2^2) E[k_1^2]) + \frac{\mu}{3h^2 \sqrt{h^2 + (R_1 + R_2)^2}} ((h^4 - 2(R_1^2 - R_2^2)^2 \\
&\quad + 2h^2(R_1^2 + R_2^2)) K[k_2^2] - (h^2 + (R_1 + R_2)^2) [h^2 - 2(R_1^2 + R_2^2)] E[k_2^2] - 3h^2(R_1 - R_2)^2 Pi[k_1^2, k_2^2]). \quad (15)
\end{aligned}$$

We consider one approximation of Eq. (15), namely axial infinity ( $h \gg R_1, R_2$ ) and have  $k_2^2 = k_4^2 \rightarrow \frac{4R_1 R_2}{h^2} \rightarrow 0$  and  $M_1 \ll M_2$ . Then

$$\begin{aligned}
M &\approx 2M_2 \approx \frac{\mu R_1 R_2 k^2}{h} \int_0^{\pi/2} \frac{\sin^2 2\theta}{1 - k^2 \sin^2 \theta} d\theta \\
&= \frac{\mu\pi(R_1 + R_2)^2}{4h} (2 - k^2 - 2\sqrt{1 - k^2}) \\
&= \frac{\mu\pi[\min(R_1, R_2)]^2}{h}, \quad (16)
\end{aligned}$$

where  $\int_0^{\pi/2} \frac{\sin^2 2\theta}{1 - k^2 \sin^2 \theta} d\theta = \frac{2 - k^2 - 2\sqrt{1 - k^2}}{k^4} \pi$  is just  $\lim_{k_i \rightarrow 0} S_i$ . This is the approximate expression (34) of inductance and mutual inductance mentioned in the literature [26]. Equation (16) calculates inductance (self-inductance) and mutual inductance when  $R_1 = R_2$  and  $R_1 \neq R_2$ , respectively. According to this equation, it is always true that  $M = L$  and  $I_\Theta = -I_P$ . This is the fundamental assumption made in Ref. [10] to estimate the growth of the MRT instability, which is equivalent to an assumption of “perfect” current induction (with 100% amplitude). In this idealized situation, the two solenoids are “tightly” matched, representing optimal coupling with maximum efficiency. However, this equation introduces significant errors in the case of a finite length.

In the case of a model with a finite axial length, both inductance and mutual inductance are accurately calculated using the exact expression for mutual inductance in Eq. (15). There is no need to rely on the approximations. However, in gaining a deeper understanding of the approximate expression in Eq. (16) for the case of an infinite axial length, for the case of a finite axial length that exceeds the radial length, which is referred to as the long solenoid approximation ( $h > R_1, R_2$ ), the exact expression in Eq. (15) for mutual inductance is expanded in a series with a large  $h$  to yield a highly accurate approximation:

$$\begin{aligned}
M &= \frac{\mu(R_1 + R_2)^3}{3h^2} (2(1 - k^2) K[k^2] - (2 - k^2) E[k^2]) \\
&\quad + \frac{\mu\pi[\min(R_1, R_2)]^2}{h} + \frac{\mu\pi R_1^2 R_2^2}{2h^3} - \frac{\mu\pi R_1^2 R_2^2 (R_1^2 + R_2^2)}{8h^5} \\
&\quad + O\left[\frac{1}{h}\right]^6. \quad (17)
\end{aligned}$$

The model with an infinite axial length in Eq. (16) evidently captures only the first-order term, resulting in considerable inaccuracies when dealing with finite lengths. When  $R_1 = R_2 = R$ , Eq. (17) degenerates into the inductance equation given as Eq. (11), which aligns with Eq. (16) in Ref. [27].

#### IV. EFFECTIVE COEFFICIENT OF CURRENT INDUCTION

As mentioned before, if “we assume the helical return can act as an infinite, ideal solenoid” [18], then the current induced on the load differs from the current in the helical RCP by only the sign; i.e.,  $I_{\Theta, \text{ideal}} = -I_P$ . A current induction effective coefficient can be defined to assess the difference between the actual induced current  $I_\Theta$  and the “ideal” induced current  $I_{\Theta, \text{ideal}}$ :  $C_I = I_\Theta / I_{\Theta, \text{ideal}} = -I_\Theta / I_P$ . When neglecting the load resistance,

$$C_I = -I_\Theta / I_P = M / L. \quad (18)$$

In the experimental configuration,  $R_2 = (1.5 \sim 2)R_1$  gradually decreases from an initial value of  $R_0$  to  $\sim 0.1R_0$  over time. Figure 5 shows the dependence of  $C_I$  on  $R_1$ , calculated using the exact equation in Eq. (15) and the long solenoid approximation in Eq. (17). The solid lines (red and black) correspond to the exact expression (15), and the dashed lines (blue and green) correspond to the

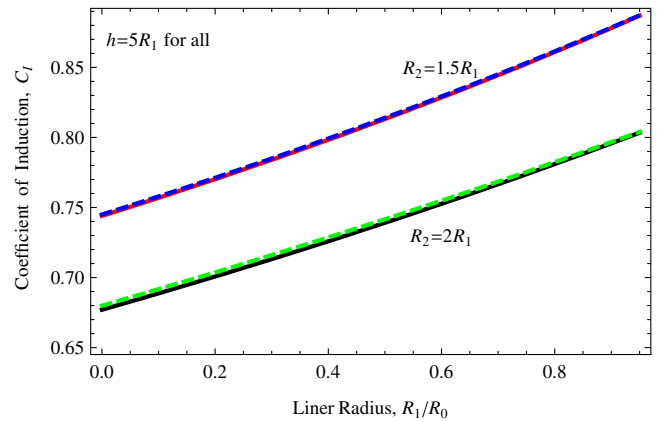


FIG. 5. Dependency of  $C_I$  on  $R_1$ . The solid lines (red and black) correspond to the exact expression (15), and the dashed lines (blue, green) correspond to the approximate expression (17).

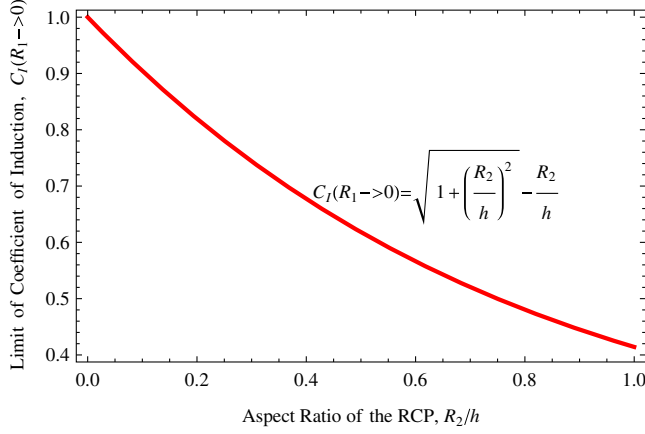


FIG. 6. Dependence of the limit value of  $C_I$  on the aspect ratio of the RCP when the load is compressed to the axis.

approximate expression (17). The respective upper bounds correspond to  $R_2 = 1.5R_1$  and the lower bounds to  $R_2 = 2R_1$ . The values obtained from the approximation closely align with those derived from the exact equation. This stands in stark contrast to the substantial deviation observed in the value obtained from the infinite length model in Eq. (16), which consistently remains at 1. The graph in Fig. 5 was generated using a fixed value of  $h = 5R_1$ .

We examined the limiting case of pinching to the center and found that even when the load is compressed to  $R_1 = 0$ ,  $C_I$  does not approach zero but remains a precise finite value  $C_I(R_1 \rightarrow 0) = \sqrt{1 + \left(\frac{R_2}{h}\right)^2} - \frac{R_2}{h}$ , as shown in Fig. 6. This value is solely determined by a structural parameter of the RCP; i.e., the aspect ratio  $R_2/h$ .

We also examined a special Z-pinch configuration in the sense of electromagnetic loading, namely the X pinch, though they are distinct in dynamics. The radial radius and axial height of the X-pinch load (center point) are very small, and we further idealize them as zero. In this case, we find  $C_I(R_1, h_1 \rightarrow 0) = 0$ , which means that the total induced current tends to zero. Despite this, the average current (line) density is finite:  $j_\Theta(R_1, h_1 \rightarrow 0) = \frac{C_I}{h_1}(R_1, h_1 \rightarrow 0) > 0$ , such as in the examples  $j_\Theta(R_1 = h_1 = 0, R_2 = 1, h_2 = 1) \approx 0.44$ ,  $j_\Theta(R_1 = h_1 = 0, R_2 = 2, h_2 = 1) \approx 0.24$ , and  $j_\Theta(R_1 = h_1 = 0, R_2 = 1, h_2 = 2) \approx 0.35$ .  $j_\Theta(R_1, h_1 \rightarrow 0)$  is a decreasing function of  $R_2$  and  $h_2$ . The average current density being nonzero indicates that the axial magnetic field still exists, for  $B_Z \approx \mu j_\Theta$ , which further suggests that the helical RCP structure can be used to suppress the instability in the X pinch and improve the temporal stability and spatiotemporal unity of hot spots. Although what exists in the X pinch may not be MRT instability but rather MHD instability or the strong coupling mode of the two, the inhibitory effect of the direction-time-varying magnetic field still exists, and the principle is that the time-averaged  $F^2$  is greater than zero as mentioned in Sec. I. In fact, the radial radius and axial height

of the X-pinch load are not zero, and the actual situation is thus better than that in the above analysis. In addition, the use of special cathode and anode plates (e.g., spirally and involutely hollowed) may further enhance this induced current and the corresponding axial magnetic field.

## V. EFFECTS OF THE ANODE AND CATHODE PLATES

The potential effects of the anode and cathode plates are considered within the framework of the LPC model. As the induced current has a pronounced nonuniform distribution along the radial direction on the anode and cathode plates, which is highly contingent on the radial position, it is challenging to accurately define a lumped inductance/mutual inductance parameter. We consider this lumped parameter an average value, presuming its value rather than calculating it. On this basis, the potential effects of the introduced factor (anode and cathode plates) are investigated.

An LPC model that comprises three elements, namely the anode and cathode plates, a helical RCP, and a magnetic pinch load (five inductance/mutual inductance parameters), is expressed as

$$\begin{pmatrix} L & M_{AK} \\ M_{AK} & L_{AK} \end{pmatrix} \begin{pmatrix} I_\Theta \\ I_{AK} \end{pmatrix} = - \begin{pmatrix} M \\ M_{AKP} \end{pmatrix} I_P, \quad (19)$$

where  $L_{AK}$  is the self-inductance of the anode and cathode plates,  $M_{AK}$  and  $M_{AKP}$  are, respectively, the mutual inductance of the plates and load and that of the plates and RCP, and the remaining variables are consistent with the previously defined notation. The solution to this equation is given by

$$I_\Theta = \frac{M_{AK}M_{AKP} - L_{AK}M}{LL_{AK} - M_{AK}^2} I_P. \quad (20)$$

An effective coefficient of current induction in the presence of anode and cathode plates is defined as  $C_{I,AK} = |I_\Theta/I_P|$ . We then have

$$\begin{aligned} C_{I,AK} &= \left| \frac{M_{AK}M_{AKP} - L_{AK}M}{LL_{AK} - M_{AK}^2} \right| \\ &= \left| \frac{M/L - M_{AK}M_{AKP}/LL_{AK}}{1 - M_{AK}^2/LL_{AK}} \right|. \end{aligned} \quad (21)$$

Let  $M_{AK}^2/LL_{AK} = a$  and  $M_{AK}M_{AKP}/LL_{AK} = b$ . Furthermore, we already have  $C_I = M/L$ , representing the effective coefficient of current induction in the absence of anode and cathode plates. On the basis of physical interpretation, we infer that  $0 \leq a, b, C_I \leq 1$ . We then have

$$C_{I,AK} = \frac{|C_I - b|}{1 - a}. \quad (22)$$

A correction factor,  $C_{AK}$ , is defined to represent the effects of the anode and cathode plates according to  $C_{AK} = C_{I,AK}/C_I$ . Let  $b/C_I = \tilde{b}$ . We then have

$$C_{AK} = \frac{|1 - \tilde{b}|}{1 - a}. \quad (23)$$

According to the values of parameters  $a$  and  $b$ ,  $C_{AK}$  can either be greater than 1 (enhancing effect) or less than 1 (weakening effect). Enhancing refers to an increase in the absolute value of the induced current amplitude relative to the case without cathode and anode plates. To maximize the enhancing effect of the anode and cathode plates on the induced current in the load, it is necessary to maximize  $a$  while simultaneously minimizing or maximizing  $b$ . This process gives rise to two optimization directions. Figure 7 shows the  $C_{AK} \geq 1$  contour lines on the  $(a, \tilde{b})$  plane. The arrows represent the two optimization directions, the colored blocks below indicate the enhancement areas in the same direction ( $I_\Theta I_P < 0$ ), and the colored blocks above indicate the enhancement areas in the opposite direction ( $I_\Theta I_P > 0$ ). Here the terms ‘‘same direction’’

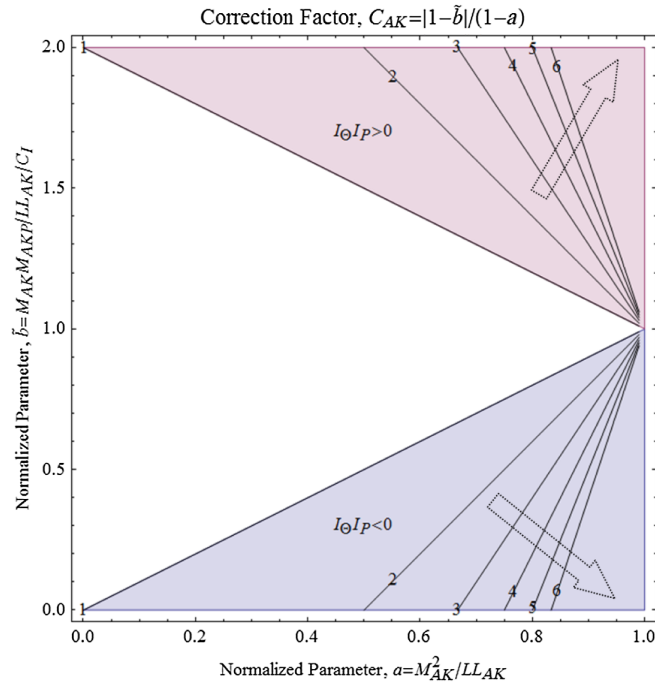


FIG. 7. Contour lines of  $C_{AK}$  in the enhancement regions and two optimization directions. In the enhancement region, relative to the case without cathode and anode plates, the absolute value of the induced current amplitude increases. As  $I_\Theta$  is opposite  $I_P$  when there are no cathode and anode plates,  $I_\Theta I_P > 0$  means that the induced current is opposite relative to the case that there are no cathode and anode plates, and vice versa.

and ‘‘opposite direction’’ are relative to the direction of induced current in the absence of anode and cathode plates. As the direction of the induced current without the cathode and anode plates is opposite the direction of the RCP current, the ‘‘same direction’’ here means the direction opposite  $I_P$  ( $I_\Theta I_P < 0$ ) and vice versa.

This analysis reveals the potential of the anode and cathode plates to enhance the current induced in the load and identifies possible optimization directions, although with some degree of uncertainty. Owing to the lack of additional information with which to constrain the precise value of  $a$  (i.e., the extent to which it approaches 1), it appears that  $C_{AK}$  may diverge. In practical configurations, it is not feasible for  $a$  to reach 1, which prevents  $C_{AK}$  from diverging.

## VI. AXIAL DISTRIBUTION OF THE INDUCED CURRENT

In accounting for the axial distribution, the expression of the induced current [i.e.,  $I_\Theta = -(M/L)I_P$ ] is formally applicable if its scalar is converted to a matrix or vector, and division is understood to be the inversion of the matrix. Now that the axial distribution is considered, the axial direction must be discretized. If we consider the ideal or near-ideal situation (i.e., the resistance is zero or very small), then the radial direction may be not discretized or only one cell is taken, which physically means that the radial skin depth is assumed to be zero or the radial scale of one cell. Such a treatment is adopted to highlight the axial distribution and temporarily ignore the radial distribution. In this discrete case, the currents  $I_\Theta$  and  $I_P$  are both column vectors and the inductances/mutual inductances  $L$  and  $M$  are both mutual inductance matrices, where the diagonal elements of  $L$  are the inductances of different subsections axially on the load. If the calculation continues like this, we find that it is impossible to obtain a converging solution; i.e., with grid refinement, the current (line) density does not converge to a constant value, and especially the current density at the endpoints is divergent. This reflects the divergent skin effect of an ideal conductor. To obtain a converged axial distribution independent of the grid, we thus need to consider the resistive effect. The departure equation for the following discussion is

$$L \frac{dI_\Theta}{dt} + RI_\Theta = -M \frac{dI_P}{dt}. \quad (24)$$

As mentioned before,  $L$  is the mutual inductance matrix of the load, and its diagonal element is the inductance of each unit in the axial direction;  $M$  is the mutual inductance matrix of the load and RCP;  $R$  is the resistance matrix of the load, which is a diagonal matrix whose elements are the resistance of each axial unit on the load; and  $I_\Theta$  and  $I_P$  are the current column vectors of the load and RCP, respectively.



Equation (24) is a system of differential algebraic equations, which can be solved numerically with software or by manually writing code. Before doing so, however, we discuss the characteristics of the solution using an approximate analytical method. The solution to Eq. (24) is written analytically as

$$I_{\Theta} = I_0 e^{-Rt/L} - e^{-Rt/L} \int_0^t e^{R\lambda/L} L^{-1} M I_p'(\lambda) d\lambda, \quad (25)$$

where the prime represents differentiation over time, the division or the  $-1$  power is understood to be matrix inversion, and the exponential function to be the matrix exponent. Equation (25) can be used directly in calculations, but this is not as efficient as numerically solving Eq. (24) owing to the matrix exponential operation. We discuss two approximate expressions of Eq. (25) that have a calculation efficiency comparable to that of the numerical solution and facilitate our discussion on the characteristics of the solution.

We derive these approximate expressions either through integration by parts or adopting a perturbation-iteration method. It is assumed here that  $L^{-1}M$  is not time dependent, or that it changes very slowly with time, especially relative to the current function. Extending this method to handle the time-dependent case more accurately would be more complex, but there are no difficulties in principle. There are two directions in which to apply the partial integration method multiple times in a chain to  $\int_0^t e^{R\lambda/L} I_p'(\lambda) d\lambda$ , which we refer to as the integral and differential directions. The integral direction refers to expressing the aforementioned integral by  $I_p$  and its further integrals, whereas the differential direction refers to expressing it by  $I_p'$  and its further differentials. In the integral notation, we follow the usual notation of differentials using  $I_p, I_p', I_p^{(3)}, \dots$  to represent the first-, second-, third-, and higher-order integrals of  $I_p$ , respectively. The expressions for the integral and differential directions are, respectively:

$$\int_0^t e^{R\lambda/L} I_p'(\lambda) d\lambda = e^{Rt/L} \left[ I_p(t) - \frac{R}{L} I_p(t) + \left(\frac{R}{L}\right)^2 I_p''(t) - \left(\frac{R}{L}\right)^3 I_p^{(3)}(t) + \dots \right] \Big|_0^t, \quad (26)$$

$$\int_0^t e^{R\lambda/L} I_p'(\lambda) d\lambda = e^{Rt/L} \left[ \frac{L}{R} I_p'(t) - \left(\frac{L}{R}\right)^2 I_p''(t) + \left(\frac{L}{R}\right)^3 I_p^{(3)}(t) + \dots \right] \Big|_0^t. \quad (27)$$

Substituting these into Eq. (25), for  $I_0 = I_p(0) = I_p'(0) = I_p''(0) = \dots = 0$ , we obtain approximate expressions that are suitable when  $Rt/L$  is small and large, respectively:

$$I_{\Theta} = -\frac{M}{L} \left( I_p - \frac{R}{L} I_p + \left(\frac{R}{L}\right)^2 I_p'' - \left(\frac{R}{L}\right)^3 I_p^{(3)} + \dots \right), \quad (28)$$

$$I_{\Theta} = -\frac{M}{R} \left[ \left( I_p' - \frac{L}{R} I_p'' + \left(\frac{L}{R}\right)^2 I_p^{(3)} + \dots \right) - e^{-Rt/L} \left( I_p'(0) - \frac{L}{R} I_p''(0) + \left(\frac{L}{R}\right)^2 I_p^{(3)}(0) + \dots \right) \right]. \quad (29)$$

The perturbation-iteration method can also be applied into two directions, namely the integral and differential directions, to obtain the above two equations. From Eq. (24), we obtain

$$I_{\Theta} = -\frac{M}{L} I_p - \frac{R}{L} I_{\Theta}, \quad (30)$$

$$I_{\Theta} = -\frac{M}{R} I_p' - \frac{L}{R} \frac{dI_{\Theta}}{dt}. \quad (31)$$

Taking the second term on the right side of these two equations as the perturbation term and substituting the previous iteration solution into the perturbation term, we obtain Eqs. (28) and (29), respectively.

Equations (28) and (29) are, respectively, suitable for the cases that  $Rt/L$  is small and large. In principle, if the definition of the integral in Eq. (28) is modified by adding a factor as the integral weight (i.e.,  $I_p = \int_0^t e^{-R\lambda/L} I_p(\lambda) d\lambda$ ), then the applicable scope of Eq. (28) is expanded. This is because the convergence of the originally defined  $I_p, I_p', I_p'', I_p^{(3)}, \dots$  sequence is insufficient, and the convergence of the modified sequence is greatly improved by the modification. This treatment is not cost-effective in practice as the matrix exponential operation is introduced and placed in the integral.

Equations (28) and (29) can be used to describe early and late behaviors, respectively. For early behaviors, only the first two terms of Eq. (28) are taken,  $I_p \approx ct I_p$ ,  $c \in (0, 1)$  is assumed, and we then have  $I_{\Theta} \approx -\frac{M}{L} (1 - \frac{cRt}{L}) I_p \approx -\frac{M}{L+cRt} I_p = -\frac{M}{L^*} I_p$ ; i.e., the axial distribution of the

induced current may be approximated easily and simply by replacing  $L$  with  $L^* = L + cRt$ .  $R$  is a diagonal matrix, and therefore, only the diagonal elements of  $L$  need to be corrected. The enhancement of diagonal elements in a matrix corresponds to the enhancement of the solution vector in the middle and the compression of its two ends. However, as the modified solution is only a minor modification of the solution in the ideal case presented at the beginning of this section, it largely preserves the characteristics of the ideal solution. The most important characteristic of the axial distribution corresponding to this solution is “high at both ends and low in the middle,” which is called the edge effect. The essence of the edge effect is the skin effect. The edge effect emphasizes that the skin effect manifests not only in the radial direction as a thin skin layer but also in the axial direction. In addition, the edge effect is regulated by the structural parameters of the load area, as discussed in detail later. For the late-stage behaviors, taking only the first term in Eq. (29), we have  $I_\Theta = -\frac{M}{R}I'_p$ . As the resistance does not directly depend on the spatial position, the characteristics of this solution are mainly determined by the mutual inductance matrix. The mutual inductance of the RCP and load is intuitively known to be “strong in the middle and weak at both ends,” and the axial distribution of the induced current corresponding to this solution is thus characterized by “high in the middle and low at both ends.” In addition to the early and late stages, we expect the existence of an intermediate stage. These stages are investigated in detail later through numerical calculations.

We now require a resistance model without introducing excessive complexity. We hope to use a simple but reasonable resistance model that has physical connotations to qualitatively or semiquantitatively discuss the axial distribution of induced current. The results and conclusions of the discussion may guide a more precise experimental design. We use the skin depth characteristic quantity  $\delta$  to measure the resistance  $R$ . The skin depth relates to a frequency or time interval. The peak moment  $\tau_m$  of the driving current waveform is used to determine a dominant frequency as the frequency in the skin depth formula. In this way, the resistance formula ( $\Theta$  current) of the discrete unit is obtained as

$$R_n = \frac{\mu\pi^2 r\delta}{2\tau_m h_n}, \quad (32)$$

where  $r$  is the radial position of the load unit,  $h_n$  is the axial height of the unit,  $R_n$  is the resistance of the unit, and the other quantities are the same as mentioned previously.

This resistance model is substituted into Eq. (24) to obtain a numerical solution. We first verify the convergence of the numerical discrete solution when the grid is refined and then evaluate the approximability of approximate expressions (28) and (29) using this high-precision numerical solution. Both approximate expressions are taken to

fifth-order terms. The approximability is measured as the maximum relative error and is obtained as less than 5%. The error in the integral-direction approximate expression (28) approximately scales as  $\varepsilon \sim \frac{\delta t^{1.1} n^{0.9}}{h^{0.5}}$ , whereas that in the differential-direction approximate expression (29) scales as  $\varepsilon \sim \frac{h^{2.2} \tau_m^{2.0}}{\delta^{0.3}}$ , where  $n$  is the number of cells, and the other quantities are the same as mentioned above. If we look only at the scaling relative to  $\delta$ , the error scaling of the differential-direction approximate expression is in-line with expectations, because the approximations are all taken to fifth-order terms and  $R$  is proportional to  $\delta$ . However, the scaling of the integral-direction approximate expression does not reach the expectation, which may be due to the insufficient convergence of the sequence  $I_p, I'_p, I''_p, I^{(3)}_p, \dots$ . The scaling of the error with respect to inductance is difficult to judge because the dependence of inductance on radial and axial dimensions is not linear. In the aforementioned discussion on error scaling, the load radius  $r$ , RCP radius  $r_p$ , and peak moment  $\tau_m$  of the drive current were fixed, and no attention was paid to the scaling of these three quantities.  $\tau_m$  is the time normalized unit, and its scaling has been included previously. The aforementioned two scalings show that the dependence on  $h$  is weak relative to that on  $\delta$ , and it is thus speculated that the dependence on  $r$ ,  $r_p$ , and  $h$  is also the same.

We finally discuss the characteristics of the solution, namely the axial distribution and time behavior of the induced current. Here  $\tau_m = r = 1$  is fixed, which is equivalent to the use of normalized units of time and length. There are then four remaining free parameters, namely  $\delta, t, h, r_p$ , which affect the axial distribution of the induced current. It is inconvenient to present a discussion for a high-dimensional parameter space. Fortunately, we find that there is an approximate invariance if we ignore minor details and focus on the main characteristics. This approximate invariance is summarized by the parameter combination  $\delta t$ . The other two parameters only weakly affect the critical values of this parameter combination and the details of the axial distribution and not the main characteristics of the axial distribution. When  $\delta t$  is small, the axial distribution is dumbbell shaped; i.e., high at both ends and low in the middle. When  $\delta t$  is large, the axial distribution is arch-shaped; i.e., high in the middle and low at both ends. When  $\delta t$  is an intermediate value, the axial distribution has a near-flat standing-wave structure; i.e., an oscillating structure with a small amplitude. These structures correspond to the early, late, and mid-term behaviors mentioned before, but here we can be more quantitative.

The critical value of  $\delta t$ , the time at which a near-flat standing-wave structure appears, is  $\sim 0.2$ , which is between 0.1 and 0.3. Such a critical value weakly depends on  $h$  and decreases slightly as  $h$  increases, whereas it is more strongly an increasing function of  $r_p$ . The details of this structure presented in the axial distribution vary slightly

depending on the different configuration parameters  $(h, r_p)$ . Figures 8 and 9 show the axial distributions of the induced current for the configurations  $(h, r_p) = (1, 2.5)$  and  $(h, r_p) = (2, 1.5)$ . These two configurations are selected to maximize the difference in details of the standing-wave structure and make the contrast most obvious.  $\delta$  corresponding to the former configuration is selected as 0.17, whereas that corresponding to the latter configuration is selected as 0.088. This treatment is conducted to align the time at which the standing-wave structure appears to  $t = 1$ , which further eliminates the effect of the current waveform. There is an effect of the load on the driving pulse waveform. Only the unidirectional effect of the driving pulse on the load is considered in our model not the bidirectional coupling. For a fixed and prescribed driving pulse waveform, the axial distribution of current density is different at different moments in the driving waveform, even for the same inductor. We chose to examine the fixed moment  $t = 1$ , i.e.,  $t = \tau_m$ , to eliminate this effect. The oscillatory structure in the two figures is a visual effect observed after magnification. In fact, the

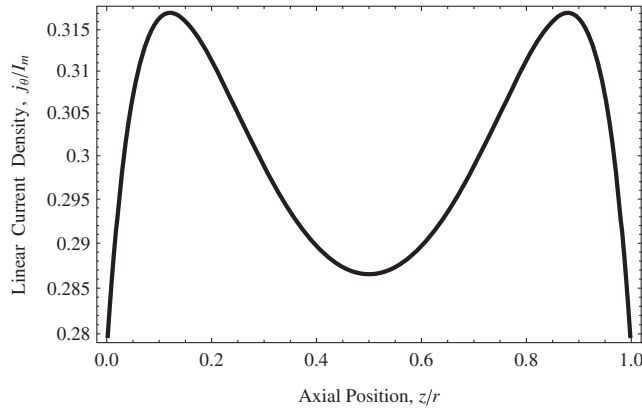


FIG. 8. Axial distribution of the induced current for the parameters  $(h, r_p, \delta, t) = (1, 2.5, 0.17, 1)$ .

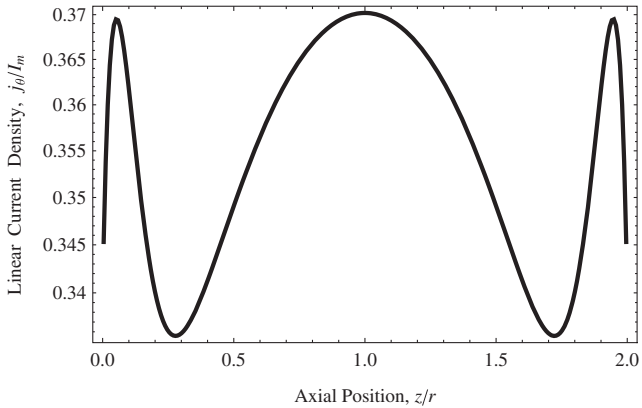


FIG. 9. Axial distribution of induced current for the parameters  $(h, r_p, \delta, t) = (2, 1.5, 0.088, 1)$ .

distribution is approximately flat, and the amplitude deviation does not exceed 5% of the median value.

The axial distribution has a dumbbell shape when  $\delta t$  is less than the critical value and an arch shape when  $\delta t$  is greater than the critical value. Two sets of parameter combinations with sharp contrast, namely  $(h, r_p, \delta) = (1, 2.5, 0.17)$  and  $(h, r_p, \delta) = (2, 1.5, 1)$ , are selected and their axial distributions at different times are compared in Figs. 10 and 11. Different colors in the two figures denote different times. From bottom to top, the first round (cycle) of red, green, blue, purple, and black lines are results for  $t = 0.1, 0.2, 0.3, 0.4,$  and  $0.5$ , respectively, and the second

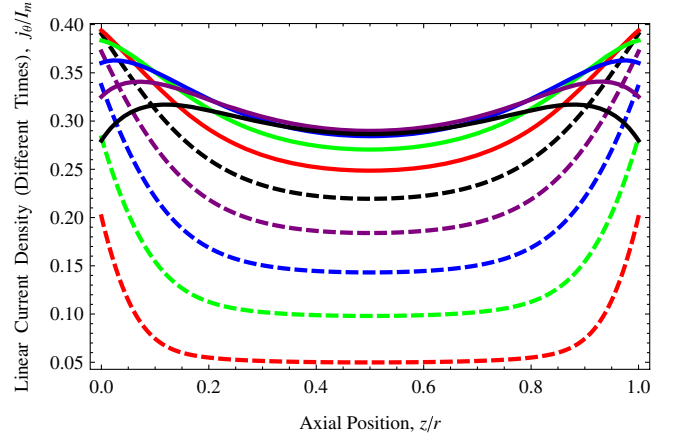


FIG. 10. Time evolution of the axial distribution of induced current for the parameter  $(h, r_p, \delta) = (1, 2.5, 0.17)$ . Different colors represent different times  $t$ . From bottom to top, the first round (cycle) of red, green, blue, purple, and black lines denotes  $t = 0.1, 0.2, 0.3, 0.4,$  and  $0.5$ , respectively, and the second round denotes  $t = 0.6, 0.7, 0.8, 0.9,$  and  $1$ .

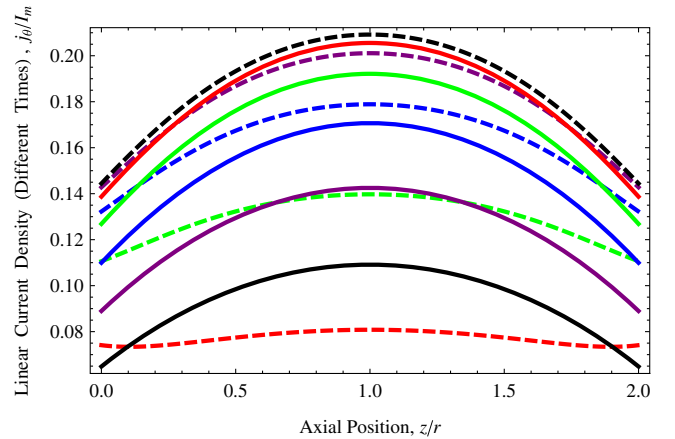


FIG. 11. Time evolution of the axial distribution of induced current for the parameter  $(h, r_p, \delta) = (2, 1.5, 1)$ . Different colors represent different times  $t$ . From bottom to top, the first round (cycle) of red, green, blue, purple, and black lines denotes  $t = 0.1, 0.2, 0.3, 0.4,$  and  $0.5$ , respectively, and the second round denotes  $t = 0.6, 0.7, 0.8, 0.9,$  and  $1$ , respectively.

round of colored lines are results for  $t = 0.6, 0.7, 0.8, 0.9,$  and  $1,$  respectively. In Fig. 10, the axial distribution is dumbbell shaped almost throughout the process, whereas in Fig. 11, it is arch-shaped almost throughout the process. We qualitatively consider the effects of these axially distributed characteristics on the dynamic driving. First, the axial distribution of the induced current evolves dynamically over time. Even if the initial driving force is designed to be approximately flat in the axial direction, it is impossible to maintain the driving force approximately flat upward on the axis throughout the process. However, we can seek sub-optimal near-flat driving; i.e., we let the near-flat drive appear at a certain intermediate moment during the implosion process, so that the overall shape of the load when pinched to the center is close to being flat. Second, it is possible to use the axial distributively induced current as shown in Fig. 10 to achieve a quasispherical implosion and further directly compress the target pellet to achieve inertial fusion, whereas that shown in Fig. 11 can be used to achieve a dumbbell-shaped implosion (if needed). The dumbbell-shaped driving force can achieve a quasispherical implosion, whereas the arch-shaped driving force can achieve a dumbbell-shaped implosion. Unlike the near-flat driving, which does not maintain a near-flat state throughout the process, these two types of driving maintain the desired shape most of the time through parameter design. In addition, the structure and shape of the cathode and anode plates and the RCP can be used to regulate the distribution and intensity of the induced current, such as in the case of spiral involute hollowed cathode and anode plates or an arc-shaped RCP.

## VII. CALCULATION OF MAGNETIC FIELDS

The total current  $I$  on the RCP is obtained by diagnosis in an experiment. The location of the diagnosis is usually a certain distance upstream of the RCP. If the number of turns of the helical RCP per axial length is  $n_c$ , the axial height of the RCP is  $h$ , and the inclination angle of the RCP is  $\theta$ , then the azimuthal current on the RCP is  $I_p = I h n_c \cos \theta$ . The induced azimuthal current  $I_\theta$  on the outer surface of the load is calculated as a function of the current induction effective coefficient  $C_I$  adopting the method used previously as  $I_\theta = I_p C_I = I h n_c C_I \cos \theta$ .  $C_I$  and  $\cos \theta$  reflect the finite length effect and inclination effect, respectively. The axial current on the load is a conduction current that is directly loaded through the electrode plates and is equal to the total current on the RCP; i.e.,  $I_z = I$ . The azimuthal and axial magnetic fields corresponding to  $I_z$  and  $I_\theta$ , respectively, are approximately calculated using their linear current densities, such that

$$B(r_1) = B_\phi \hat{\phi} + B_z \hat{z} \approx \mu_0 I [1/2\pi r_1 \hat{\phi} + n_c C_I \cos \theta \hat{z}], \quad (33)$$

where  $\cos \theta$  can be further expressed by  $n_c$ . When the RCP encircles one turn, it advances a distance in the axial

direction of  $1/n_c$  and a distance in the arc direction of  $2\pi r_2$ , such that  $\cos \theta = \frac{2\pi r_2 n_c}{\sqrt{1+(2\pi r_2 n_c)^2}}$ . Here  $r_1$  is the radius of the load and  $r_2$  is the radius of the RCP. If the axial discrete model is used to calculate the induced current, then the second term in Eq. (33) can be directly substituted with its linear current density, but it is noted that  $\cos \theta$  should be considered when setting the current excitation source. If the inclination angle is ignored ( $\theta \rightarrow 0$ ) and an infinite length is assumed ( $C_I \rightarrow 1$ ), Eq. (33) becomes the formulas given in the literature [10,15,18,19]. However, the following comparisons show that the correction of the inclination angle and finite length effect are necessary.

We conduct three comparisons taking data from the literature [18,19]. In the first comparison, according to Fig. 1(c) in [19],  $n_c \approx \frac{1/4}{19.4}$ ,  $r_1 = 3.175$ ,  $r_2 = 8.9$  are taken. The inclination angle of the magnetic field calculated as per Eq. (33) is  $\phi_B = \arctan(B_z/B_\phi) \approx 6.4^\circ$ . The error is approximately 9% relative to  $7.0^\circ \pm 0.7^\circ$  given in the paper based on image diagnosis in Fig. 3(c). If the formula given in the literature [10,15,18,19] is used, where  $\cos \theta$  and  $C_I = 0.74$  are not considered, then  $\phi_B \approx 14.4^\circ$ , which differs greatly from the value of  $7.0^\circ$ .

The second comparison refers to Fig. 1 of Ref. [18]. In this case,  $n_c = 0.8$ ,  $r_1 = 0.3$ ,  $r_2 = 0.8$ ,  $C_I \approx 0.646$ . If  $\cos \theta$  and  $C_I$  are ignored, then the driving magnetic field ratio is  $\Xi = B_z/B_\phi \approx 1.5$ . If  $\cos \theta$  and  $C_I$  are considered, then  $\Xi \approx 0.94$ . If the peak value in Fig. 1(c) is used as the benchmark, then the relative error is approximately 34%.

The third comparison is carried out using the data presented in Figs. 9(b) and 10 of Ref. [18]. We extract the  $\Xi$  data of the outer surface of the liner in Fig. 9(b) and the  $\Xi$  data in Fig. 10 and present them in Fig. 12 as blue and green lines, respectively. The  $\Xi$  data calculated as per Eq. (33) and that calculated as per the formulas previously

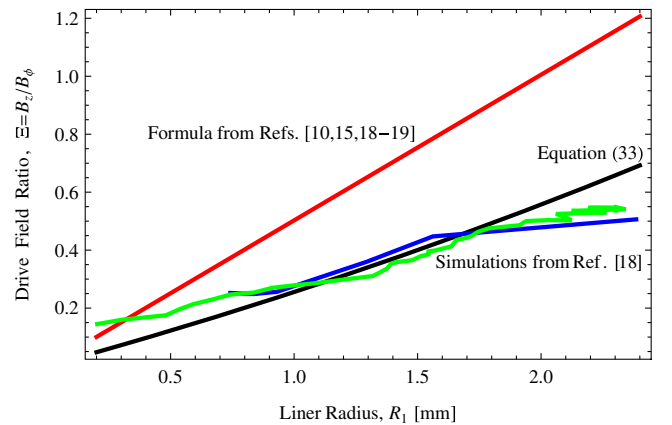


FIG. 12. Comparison of the driving magnetic field ratio  $\Xi = B_z/B_\phi$  given by simple formulas and advanced numerical simulations. Blue line: extracted from Fig. 9(b) of [18], numerical simulation; Green line: extracted from Fig. 10 of [18], numerical simulation; Black line: calculated as per Eq. (33); Red line: calculated as per the formulas in [10,15,18,19].

given in the literature [10,15,18,19] (with  $\cos\theta$  and  $C_I$  ignored) are presented in Fig. 12 by black and red lines, respectively. As intuitively shown in this figure, Eq. (33) is closer to the advanced numerical simulation results of Ref. [18], and the correction of the inclination angle and finite length effect is very necessary. It is necessary to update those theoretical evaluations of the dynamics, instability, and driver-target coupling of dynamic screw pinches based on old formulae. Results in this paper can also be extended to improve the current circuit models explained in the literature [28,29]. However, these contents are beyond the scope of this paper.

### VIII. CONCLUSION

The current azimuthally induced on the outer surface of a load located in a helical RCP structure deviates significantly from the “perfect” induced current (100% amplitude:  $I_\Theta = -I_P$ ). The effective coefficient of current induction,  $C_I$ , is notably less than 1. However,  $C_I$  does not approach zero even when the load is compressed to  $R_1 = 0$ . Instead, it remains a finite value that is solely determined by the aspect ratio of the RCP. For a point-like  $X$  pinch, the axial magnetic field does not tend to zero but is a finite value, though  $C_I$  tends to zero. This result may be used to suppress instability in an  $X$  pinch and improve the time stability and spatiotemporal unity of hot spots.

A three-element LPC model was used to analyze the possibility of anode and cathode plates enhancing azimuthal induced current on the load. Optimization involves maximizing  $a$  while simultaneously minimizing or maximizing  $b$ .

There is an approximate invariance in the axial distribution and time behavior of the induced current. The parameter combination  $\delta t$  of skin depth  $\delta$  and time  $t$  related to magnetic diffusion can be used to well summarize this approximate invariance. That is, when  $\delta t$  is near 0.2, or between 0.1 and 0.3, the axial distribution presents a nearly flat standing wave structure; when  $\delta t$  is less than this critical value, the axial distribution is dumbbell shaped; and when  $\delta t$  is larger than this critical value, the axial distribution is arch shaped. Correspondingly,  $\delta t$  can be designed to be at, below, or above the critical region during most of the implosion process to obtain a nearly flat, quasispherical, or dumbbell-shaped implosion, respectively. A semiquantitative design criterion was provided in this paper. More accurate design and optimization require the combination of implosion dynamics and dynamic material properties. That work and the exploration of regulation through cathode and anode plates and the RCP are left for future studies.

### ACKNOWLEDGMENTS

This work was supported by the National Natural Science Foundation of China under Grant No. 12075226. We wish to

thank the reviewers for their valuable comments and suggestions. The first author S.-C. Duan also wishes to thank Dr. J.-K. Dan for helpful discussions.

- 
- [1] M. A. Liberman, J. S. De Groot, A. Toor, and R. B. Spielman, *Physics of High-Density Z-Pinch Plasmas* (Springer-Verlag, New York, 1999).
  - [2] D. D. Ryutov, M. S. Derzon, and M. K. Matzen, The physics of fast Z pinches, *Rev. Mod. Phys.* **72**, 167 (2000).
  - [3] M. G. Haines, A review of the dense Z pinch, *Plasma Phys. Controlled Fusion* **53**, 093001 (2011).
  - [4] L. Rayleigh, Investigation of the character of the equilibrium of an incompressible heavy fluid of variable density, *Proc. London Math. Soc.* **14**, 170 (1882).
  - [5] G. I. Taylor, The instability of liquid surfaces when accelerated in a direction perpendicular to their planes. I, *Proc. R. Soc. A* **201**, 192 (1950).
  - [6] D. J. Lewis, The instability of liquid surfaces when accelerated in a direction perpendicular to their planes. II, *Proc. R. Soc. A* **202**, 81 (1950).
  - [7] D. H. Sharp, An overview of Rayleigh–Taylor instability, *Physica (Amsterdam)* **12D**, 3 (1984).
  - [8] S. Duan, A research on magneto-Rayleigh–Taylor instability in dynamic Z pinches, NNSFC, Beijing, China, Proposal Report No. 1140050776, 2014.
  - [9] S. Duan and D. Li, Private communication for discussion on the results by email, 2016.
  - [10] P. F. Schmit, A. L. Velikovich, R. D. McBride, and G. K. Robertson, Controlling Rayleigh–Taylor instabilities in magnetically driven solid metal shells by means of a dynamic screw pinch, *Phys. Rev. Lett.* **117**, 205001 (2016).
  - [11] S. Duan, W. Xie, J. Cao, and D. Li, Magneto-Rayleigh–Taylor instability driven by a rotating magnetic field, *Phys. Plasmas* **25**, 042701 (2018).
  - [12] S.-C. Duan, L. Yang, B. Xiao, M.-X. Kan, G.-H. Wang, and W.-P. Xie, Magneto-Rayleigh–Taylor instability driven by a rotating magnetic field: Cylindrical liner configuration, *IEEE Trans. Plasma Sci.* **47**, 4547 (2019).
  - [13] S. A. Sorokin and S. A. Chaikovskii, Achieving high degrees of stable radial compression of plasma liners, *Plasma Phys. Rep.* **19**, 444 (1993).
  - [14] S. A. Sorokin and S. A. Chaikovskiy, Imploding liner stabilization experiments on the SNOP-3 generator, *AIP Conf. Proc.* **299**, 83 (1994).
  - [15] S. A. Sorokin, Gas-puff liner implosion in the configuration with helical current return rods, *Plasma Phys. Rep.* **39**, 139 (2013).
  - [16] L. Atoyán, D. A. Hammer, B. R. Kusse, T. Byvank, A. D. Cahill, J. B. Greenly, S. A. Pikuz, and T. A. Shelkovenko, Helical plasma striations in liners in the presence of an external axial magnetic field, *Phys. Plasmas* **23**, 022708 (2016).
  - [17] P.-A. Gourdain, M. B. Adams, J. R. Davies, and C. E. Seyler, Axial magnetic field injection in magnetized liner inertial fusion, *Phys. Plasmas* **24**, 102712 (2017).
  - [18] G. A. Shipley, C. A. Jennings, and P. F. Schmit, Design of dynamic screw pinch experiments for magnetized liner inertial fusion, *Phys. Plasmas* **26**, 102702 (2019).

- [19] P. C. Campbell, T. M. Jones, J. M. Woolstrum, N. M. Jordan, P. F. Schmit, J. B. Greenly, W. M. Potter, E. S. Lavine, B. R. Kusse, D. A. Hammer, and R. D. McBride, Stabilization of liner implosions via a dynamic screw pinch, *Phys. Rev. Lett.* **125**, 035001 (2020).
- [20] G. G. Zukakishvili, K. N. Mitrofanov, E. V. Grabovskii, and G. M. Oleinik, Measurements of the axial magnetic field during the implosion of wire arrays in the Angara-5-1 facility, *Plasma Phys. Rep.* **31**, 652 (2005).
- [21] F. Suzuki-Vidal, S. V. Lebedev, S. N. Bland, G. N. Hall, A. J. Harvey-Thompson, J. P. Chittenden, A. Marocchino, S. C. Bott, J. B. A. Palmer, and A. Ciardi, Effect of wire diameter and addition of an axial magnetic field on the dynamics of radial wire array Z-pinch, *IEEE Trans. Plasma Sci.* **38**, 581 (2010).
- [22] S. A. Slutz, C. A. Jennings, T. J. Awe, G. A. Shipley, B. T. Hutsel, and D. C. Lamppa, Auto-magnetizing liners for magnetized inertial fusion, *Phys. Plasmas* **24**, 012704 (2017).
- [23] G. A. Shipley, T. J. Awe, B. T. Hutsel, S. A. Slutz, D. C. Lamppa, J. B. Greenly, and T. M. Hutchinson, Megagauss-level magnetic field production in cm-scale auto-magnetizing helical liners pulsed to 500 kA in 125 ns, *Phys. Plasmas* **25**, 052703 (2018).
- [24] G. A. Shipley, T. J. Awe, B. T. Hutsel, J. B. Greenly, C. A. Jennings, and S. A. Slutz, Implosion of auto-magnetizing helical liners on the Z facility, *Phys. Plasmas* **26**, 052705 (2019).
- [25] A. L. Velikovich and P. F. Schmit, Bell-Plesset effects in Rayleigh-Taylor instability of finite-thickness spherical and cylindrical shells, *Phys. Plasmas* **22**, 122711 (2015).
- [26] N. Miura and K. Nakao, Computer analysis of megagauss field generation by condenser bank discharge, *Jpn. J. Appl. Phys.* **29**, 1580 (1990).
- [27] Y. Zhang, Calculation of mutual inductance between two coaxial solenoids, *Coll. Phys.* **1**, 15 (1989).
- [28] R. D. McBride and S. A. Slutz, A semi-analytic model of magnetized liner inertial fusion, *Phys. Plasmas* **22**, 052708 (2015).
- [29] J. L. Giuliani and R. J. Comisso, A review of the gas-puff Z pinch as an x-ray and neutron source, *IEEE Trans. Plasma Sci.* **43**, 2385 (2015).